JOURNAL OF GEOPHYSICAL RESEARCH, VOL. 115, A06204, doi:10.1029/2009JA014828, 2010

Click Here for Full Article

Foreshock bubbles and their global magnetospheric impacts

N. Omidi,[1] J. P. Eastwood,[2] and D. G. Sibeck[3]

Received 24 August 2009; revised 4 December 2009; accepted 21 January 2010; published 11 June 2010.

[1] We employ 2.5-D electromagnetic, hybrid simulations that treat ions kinetically via particle-in-cell methods and electrons as a massless fluid to study the formation and properties of a new structure named the foreshock bubble upstream from the bow shock. This structure forms due to changes in the interplanetary magnetic field (IMF) associated with solar wind discontinuities and their interaction with the backstreaming ions in the foreshock prior to these discontinuities encountering the bow shock. The leading edge of the foreshock bubble consists of a fast magnetosonic shock and the compressed and heated plasma downstream of the shock. The leading edge surrounds the core which consists of a less-dense and hotter plasma and lower magnetic field strength. Ultra low frequency turbulence is present in both the outer and core regions of the foreshock bubbles. The size of the foreshock bubble transverse to the flow direction scales with the width of the ion foreshock and at Earth corresponds to tens of R_E. The size along the flow depends on the age of the bubble and grows with time. Although they expand sunward, foreshock bubbles are carried antisunward by the solar wind, and for small IMF cone angles (angle between IMF and solar wind flow) when the foreshock lies upstream of the dayside magnetosphere they collide with the bow shock. This collision is shown to have significant magnetospheric impacts. Upon encountering the bow shock, the low pressures within the core of the bubble result in the reversal of the magnetosheath flow from antisunward to sunward direction. This in turn results in the outward motion of the magnetopause and expansion of the dayside magnetosphere. The interaction is found to noticeably impact the density and energy of trapped radiation belt ions and plasma injection into the cusp. Foreshock bubbles are found to be highly effective sites for ion reflection and acceleration to high energies via first- and second-order Fermi acceleration. The interaction of the foreshock bubble with the bow shock results in the release of energetic ions into the magnetosheath. Some of these ions are subsequently injected into the cusp.

Citation: Omidi, N., J. P. Eastwood, and D. G. Sibeck (2010), Foreshock bubbles and their global magnetospheric impacts, *J. Geophys. Res.*, *115*, A06204, doi:10.1029/2009JA014828.

1. Introduction

[2] Collisionless dissipation processes at the bow shock result in reflection/leakage of ions into the upstream forming the ion foreshock region [*Asbridge et al.*, 1968; *Greenstadt et al.*, 1968, 1980; *Gosling et al.*, 1978; *Paschmann et al.*, 1979; *Bonifazi et al.*, 1980a, 1980b]. Observations have established that the backstreaming ions form a variety of velocity distribution functions that range from field-aligned beams to highly scattered and heated distribution functions called diffuse ions [see *Fuselier*, 1995]. Also, a variety of ultralow frequency (ULF) waves such as 30 s sinusoidal and shocklets have been observed in association with the backstreaming ions [e.g. *Hoppe et al.*, 1981; *Russell and Hoppe*, 1983; *Eastwood et al.*, 2005; *Mazelle et al.*, 2007]. Recently, *Blanco-Cano et al.* [2009] have discovered structures in Cluster data called foreshock cavitons that form through nonlinear ULF wave interactions [*Lin*, 2003; *Omidi*, 2007] and are associated with drops in density and magnetic field strength by as much as ~50%. Convection of both ULF waves and nonlinear structures into the bow shock results in a turbulent magnetosheath impacting magnetopause dynamics and transport processes such as reconnection. In addition to the generation of turbulence, other kinetic processes associated with the bow shock are responsible for major changes in the magnetopause and the associated magnetospheric processes. For example, hot flow anomalies (HFAs) are formed as a result of the interaction between tangential or rotational discontinuities (TDs or RDs) marked by inward-pointing electric fields, on one or both sides of discontinuity, and the bow shock [e.g. *Schwartz*, 1995; *Schwartz et al.*, 1988, 2000; *Thomsen et al.*, 1986, 1988, 1993; *Paschmann*

[1]Solana Scientific Inc., Solana Beach, California, USA.
[2]Space Sciences Laboratory, University of California, Berkeley, California, USA.
[3]NASA Goddard Space Flight Center, Greenbelt, Maryland, USA.

Copyright 2010 by the American Geophysical Union.
0148-0227/10/2009JA014828

et al., 1988; *Burgess*, 1989; *Thomas et al.*, 1991; *Sibeck et al.*, 1998, 1999, 2000; *Lin*, 1997, 2002; *Lucek et al.*, 2004; *Omidi and Sibeck*, 2007; *Facskó et al.*, 2008; *Eastwood et al.*, 2008; *Jacobsen et al.*, 2009]. *Schwartz et al.* [2000] estimate the rate of HFA occurrence to be about three per day. *Sibeck et al.* [1999] examined the response of the magnetosphere to a HFA and found evidence for the deformation of the magnetopause and its outward motion by 5 R_E in 7 min. More recently, Thermal Emission Imaging System (THEMIS) multispacecraft observations have established a direct link between formation of HFAs and significant magnetospheric activities [*Eastwood et al.*, 2008; *Jacobsen et al.*, 2009]. *Eastwood et al.* [2008] showed that HFAs have a complex structure in the magnetosheath and are associated with pressure pulses that upon encountering the magnetopause initiate a series of processes which result in the observed magnetic perturbations on the ground. *Jacobsen et al.* [2009] reported an event demonstrating that the formation of an HFA at the bow shock is associated with a 4.8 R_E outward displacement of the magnetopause in 59 s, resulting in a mean outward velocity of ~518 km/s. The instantaneous velocity along the normal reached 800 km/s during this event. They also found a large bulge on the magnetopause traveling tailward at a speed of 355 km/s. This in turn, resulted in the generation of field-aligned currents and traveling convection vortices which were detected by the ground magnetometers.

[3] Given the large number and variety of solar wind discontinuities, the question that arises is if they result in the formation of structures other than HFAs at or upstream of the bow shock. For example, *Burlaga* [1969] reports observations of 10 to 50 directional discontinuities a day in the solar wind. In this paper we show results from 2.5-D hybrid (kinetic ions, fluid electrons) simulations that indicate the presence of a new structure we name foreshock bubble (FB). Foreshock bubbles form as a result of the change in the interplanetary magnetic field direction associated with solar wind discontinuities and its interaction with the backstreaming ion beams in the foreshock. Unlike HFAs, foreshock bubbles are formed prior to the interaction of the discontinuity with the bow shock itself. Also in contrast to HFAs, formation of foreshock bubbles is not tied to the direction of the motional electric field on either side of the discontinuity. Instead, upon encountering the discontinuity, the ion beam is deflected in response to the change in the magnetic field direction. The interaction between the deflected beam and the solar wind results in the formation of a fast magnetosonic shock wave that expands sunward with time and a central core region consisting of hot and tenuous plasma. Foreshock bubbles are carried antisunward by the solar wind and, as we show here, during small interplanetary magnetic field (IMF) cone angles (angle between IMF and flow velocity) collide with the dayside bow shock. This collision results in sunward flows in the magnetosheath and outward expansion of the magnetopause and the dayside magnetosphere. The interaction also impacts particle injection into the cusp by disrupting high-latitude reconnection and density and energy of trapped radiation belt ions.

[4] The structure of the paper is as follows. Section 2 describes the two hybrid models used in this study. In one model, the formation and structure of the foreshock bubbles are investigated in isolation allowing us to examine the impacts of ion beam properties and IMF orientation. The second model is global in nature and includes the bow shock and the magnetosphere allowing us to examine the magnetospheric impacts of the FB. In section 3 we examine the properties of the foreshock bubbles in isolation, whereas section 4 looks at their interaction with the magnetosphere. Section 5 provides a summary and conclusions.

2. Hybrid Simulation Model

[5] The main tools of investigation in this study are 2.5-D (2-D in space and 3-D in currents and electromagnetic fields) local and global hybrid simulations used extensively in the past. In electromagnetic hybrid codes, ions are treated as macroparticles and consist of one or more species (e.g., differing mass, charge), whereas electrons are treated as a massless, charge-neutralizing fluid [see, e.g., *Winske and Omidi*, 1993, 1996]. The local model is used to understand the structure of the foreshock bubble and the roles of ion beam density, velocity, width, and IMF direction on its formation. The global model is used to investigate the impacts of the FB collision with the bow shock and the magnetosphere. In the following we describe each of these models.

[6] The local simulation box lies in the X-Y plane with X along the solar wind flow and with initial IMF in the simulation plane. Nonperiodic boundary conditions are used in both X and Y directions. The size of the box corresponds to 1000 ion skin depths (c/ω_p, where c is the speed of light and ω_p is the ion plasma frequency) in the X direction and between 500 and 2000 c/ω_p in the Y direction. A solar wind type plasma is continuously injected from the $X = 0$ boundary and allowed to leave the system from the remaining three boundaries. In addition to the solar wind, a finite-sized (in both X and Y directions) ion beam with velocity equal but opposite in direction to that of the solar wind is present for $50 < X < 1000$. We use a beam temperature equal to that of the solar wind. Ion beams with width ranging from 100 to 300 c/ω_p are used to investigate the size and scaling properties of the foreshock bubble.

[7] The direction of the IMF in the box changes due to a rotational discontinuity initially located at $X = 30$ c/ω_p with normal in the X direction. To examine the impacts of the IMF direction, cone angles ranging between 0° and 50° are considered for $X > 30$. In the case of 0° cone angle, behind the RD ($X < 30$), the magnetic field has a Z component with half the strength of the X component which stays the same as in the region $X > 30$ due to conservation of the normal component of the magnetic field. For all other cone angles, the Y component of IMF is rotated by 90° behind the RD so that it falls along the Z direction. No other changes in plasma conditions take place across the RD. Solar wind ion and electron betas (ratio of kinetic to magnetic pressure) of 0.5 and 1, respectively, and flow speeds ranging from 6 to 12 V_A (Alfven speed) have been considered in the study. Similarly, beam densities ranging between 0.5% and 2% of the solar wind density have been used. The cell size is 1 ion skin depth with 15 particles per cell representing the solar wind protons. We also use 15 particles per cell for the backstreaming proton beam but give their contributions to plasma density a smaller weight to correspond to the beam density chosen for the run. The global hybrid model to be

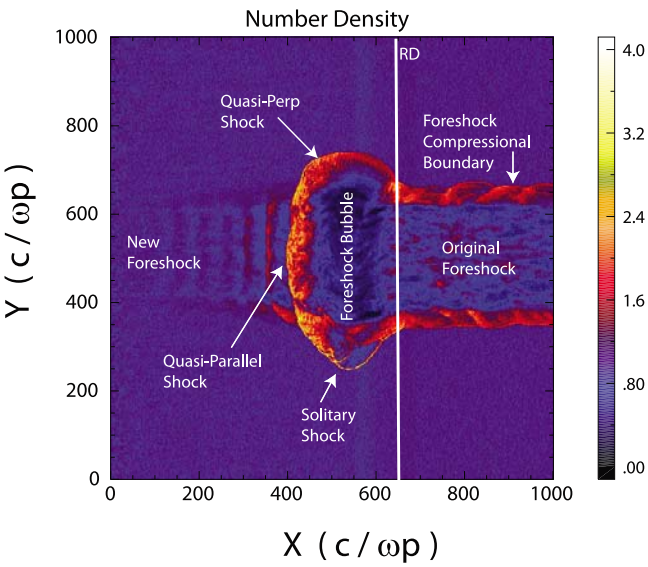

Figure 1. Color intensity plot of density normalized to solar wind value illustrates the structure of the foreshock bubble.

utilized in this study has been used extensively in the past [e.g., *Omidi et al.*, 2004, 2005, 2006, 2009a, 2009b; *Omidi and Sibeck*, 2007; *Blanco-Cano et al.*, 2006a, 2006b; 2009; *Sibeck et al.*, 2008]. The basic model consists of a dipole inside a sphere with its surface representing the ionospheric boundary where various boundary conditions can be applied. For the objectives of this study, a perfect conducting surface is adequate and will be utilized. Initially, a solar wind type plasma (electron and ion betas of 1 each and flow speed of 12 V_A) is uniformly loaded in the system except for inside the ionospheric boundary. This plasma is continuously injected from the left-hand boundary throughout the whole run. The remaining boundaries remain open for the plasma to leave. Similarly, open boundary conditions are applied for the electromagnetic fields so that excited waves and turbulence in the system leave through these boundaries. As in the local simulations the box lies in the X-Y plane with X along the solar wind flow direction (Sun–Earth line) and the dipole moment in the Y direction. The simulation box extends 1400 ion skin depths in the X direction and 1200 in the Y direction with cell size of 1 ion skin depth. Regarding the number of particles, we use 15 particles per cell for the solar wind protons and utilize particle-splitting schemes [*Lapenta*, 2002] for the backstreaming ions in the foreshock to improve their statistics. Specifically, each backstreaming ion is split into 16 particles with their mass and charge reduced by a factor of 16.

[8] Initially, we use a radial IMF to generate the bow shock and the magnetosphere. We then launch an RD from the left boundary with normal along the X direction. As in the local simulations, behind the RD a Z component of the magnetic field is present with strength equal to half the radial magnetic field. As the RD propagates, it interacts with the backstreaming ions in the foreshock and forms a foreshock bubble which is carried by the solar wind until it interacts with the bow shock and the magnetosphere. We note that to optimize the computational resources, the simulated magnetospheres are smaller (factors of 5–10) than the Earth's magnetosphere. On the other hand, the simulated plasma parameters and characteristic time and spatial scales such as gyroperiod or ion skin depth are the same as those in solar wind and magnetosphere. This implies that the simulations are capable of generating plasma and field values and characteristic scales that can be directly compared to observations at the Earth's bow shock. However, the size of the simulated structures and their ratio to the size of the magnetosphere is in general different from the actual sizes and ratios at Earth. In order to understand the size of the FBs at the Earth's bow shock, this study entails investigation of scaling properties of the foreshock bubbles. It is shown that the size of FBs perpendicular to the flow direction scales with the width of the ion foreshock, and as a result the simulated FBs are about 5–10 times smaller than those at Earth. However, the ratio of the size of the FB to the magnetosphere is the same for both simulated and the Earth's magnetosphere. As demonstrated in our earlier studies, the physical processes occurring in smaller bow shocks and magnetospheres are similar to those at the Earth's magnetosphere, and much can be learned from these simulations including scaling properties of various magnetospheric processes [e.g., *Omidi et al.*, 2004, 2005, 2006, 2009a, 2009b; *Omidi and Sibeck*, 2007; *Blanco-Cano et al.*, 2006a, 2006b; 2009; *Sibeck et al.*, 2008].

3. Properties of the Foreshock Bubble

[9] In this section, we use the results of local hybrid simulations to examine the formation and properties of the foreshock bubbles. We begin by looking at the structure of the FB, followed by its size and scaling properties and the effects of the IMF cone angle.

3.1. Structure of the Foreshock Bubble

[10] Figure 1 shows the density (normalized to solar wind value) in the X-Y plane corresponding to a run with solar wind velocity of 12 V_A and beam density 2% of the solar wind and beam width of 200 ion skin depth. By this time in the run ($\Omega t = 50$, where Ω is the proton gyrofrequency), the RD is at $X \sim 630$. The region to the right of the RD corresponds to the original ion beam ("foreshock") where wave particle interactions have resulted in the formation of foreshock cavitons. The top and bottom boundaries between the foreshock and the solar wind are associated with density enhancements. This boundary labeled the foreshock compressional boundary (FCB) was recently discovered in global hybrid simulations [*Sibeck et al.*, 2008; *Omidi et al.*, 2009a], and its existence has been verified in spacecraft data. A detailed discussion of the properties of FCBs and their dependence on solar wind conditions (i.e., Mach number and IMF cone angle) is given by *Omidi et al.* [2009a].

[11] The foreshock bubble formed in this run can be seen on the left side of the RD. The outer layer of the FB consists of a fast magnetosonic shock wave with the associated heated and decelerated plasma downstream of it. This shock wave corresponds to quasi-perpendicular and quasi-parallel geometries as indicated in Figure 1. The lower part of the shock wave labeled solitary shock corresponds to quasi-perpendicular geometry, but the shock has properties that are different from typical quasi-perpendicular shocks as

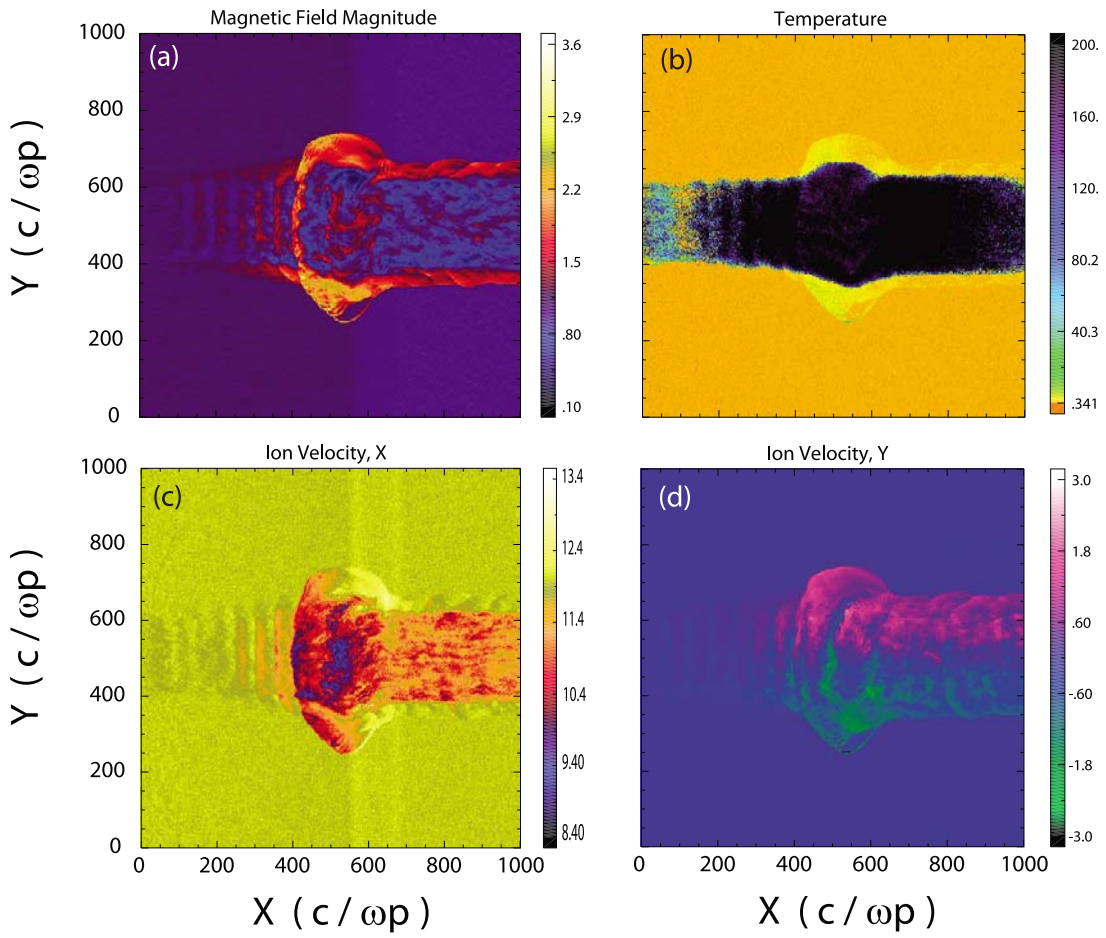

Figure 2. Plots of magnetic field, ion temperature and velocities in X and Y directions for the same run as in Figure 1. The magnetic field and temperature are normalized to their corresponding values in the solar wind, while the velocities are normalized to the Alfven speed in the solar wind.

discussed in detail by *Omidi and Sibeck* [2007]. Ion reflection and leakage at the quasi-parallel part of this shock results in the formation of a new foreshock with ULF wave properties that are different from those in the original foreshock. This difference is due to changes in the beam properties in the new foreshock. The core region of the foreshock bubble consists of plasma with density below that of the solar wind. Variations in density associated with the ULF waves present in the core are also visible in Figure 1.

[12] To further examine the structure of the foreshock bubble, Figure 2 shows the total magnetic field strength, ion temperature, and velocities in X and Y directions. The magnetic field and temperature are normalized to their corresponding values in the solar wind while the velocities are normalized to the Alfven speed in the solar wind. As can be seen, the magnetic field structure is very similar to the density and is associated with enhancements above the solar wind values in the outer layer and drops to values below the IMF strength in the core region. Variations in the field strength associated with ULF waves are also visible in the core region. The ion temperature in Figure 2b shows the heating associated with the FB shock wave. However, because the temperature is calculated as the moment of the total ion distribution function, the presence of ion beams in the foreshock and the core region increases the temperature even when solar wind is not heated. For this reason, it will be more instructive to examine the evolution of the ion distribution function as described in this paper. Figure 2c shows clear evidence for solar wind deceleration downstream of the FB shock wave and in the core region of the foreshock bubble. Similarly, Figure 2d shows plasma diversion associated with the foreshock bubble.

[13] Figure 3 shows the ion velocity distribution functions in V_X and V_Y at five positions indicated by the arrows. Figure 3a shows the solar wind and an ion beam far upstream of the foreshock bubble. The ion beam is associated with reflected/leaking ions from the quasi-parallel part of the shock associated with the FB and looks similar to the intermediate ion beams in the foreshock. Figure 3b shows the distribution function just upstream of the bubble, which consists of the solar wind and a highly scattered beam that looks like the diffuse ion beams in the foreshock. Figure 3c shows the distribution function within the core of the FB. It illustrates that the peak in the distribution function (maximum value of the color bar) is much smaller than those in the other panels and that the core is less dense and much hotter than the solar wind plasma. Figure 3d corresponds to the distribution function in the original foreshock region and shows the presence of the solar wind and a hotter population of ions that is associated with the scattered ion beam.

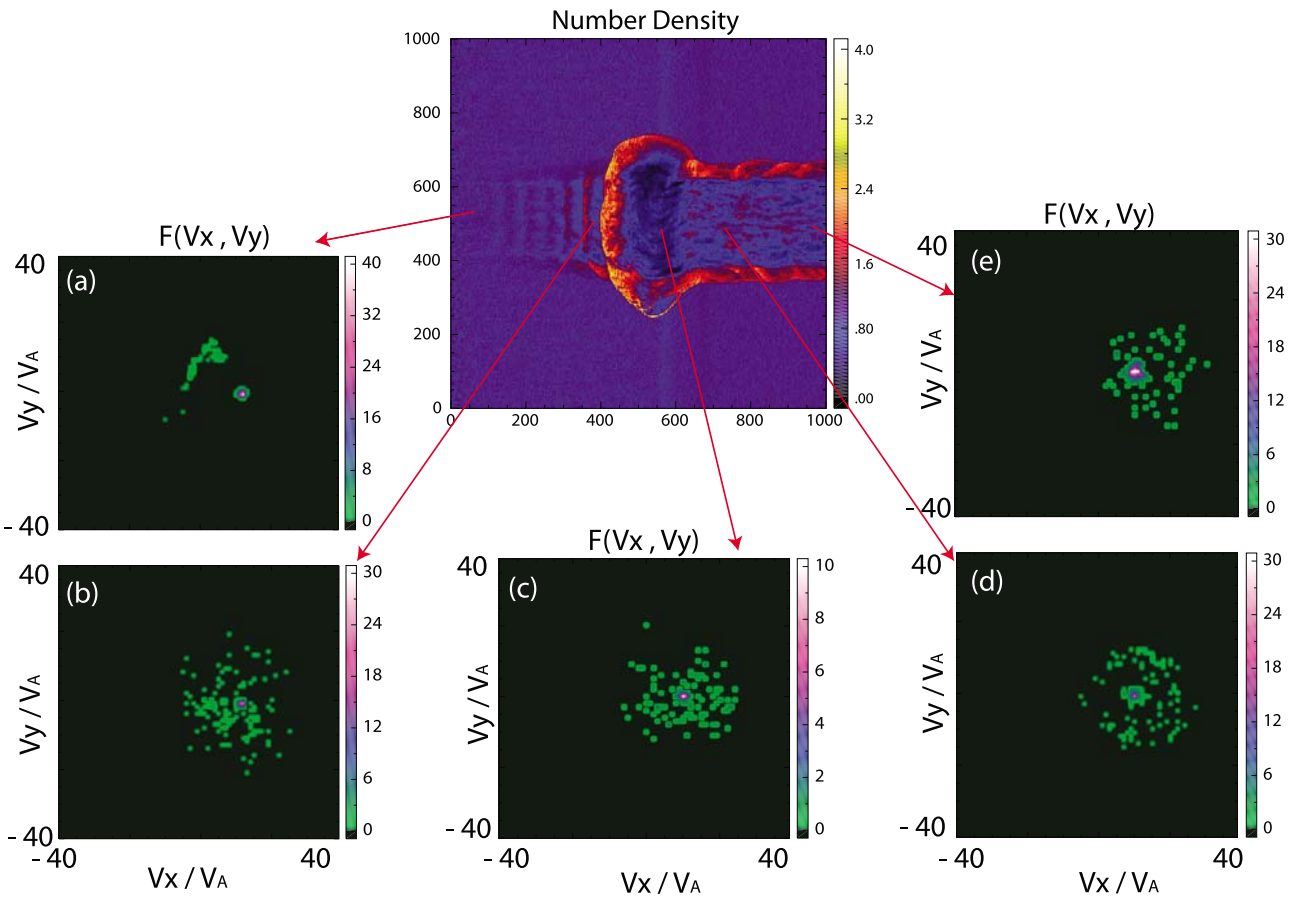

Figure 3. Plots of ion velocity distribution function in V_X and V_Y at five different locations indicated by the arrows from the density plot.

Examination of these ions shows that most have positive V_X (i.e., they are moving in the antisunward direction). As illustrated in Figure 3e, this effect is even more pronounced further downstream and indicates the reflection of the originally sunward-moving ion beam by the foreshock bubble. Note that because the ion beam is not refurbished during the run, the presence of sunward-moving ions in Figure 3d and 3e is indicative of reflection of antisunward-moving ions by the ULF waves in the original foreshock. This is because by this time in the run (Ωt = 50), the beam particles starting at X = 1000 would have moved upstream by 600 ion skin depths, and no sunward-moving particles would have been left in the regions corresponding to Figures 3d and 3e. Both the fact that foreshock bubbles are convected by the solar wind and result in ion reflection and the presence of the foreshock bubbles in the foreshock make ULF waves highly effective accelerators of particles through first- and second-order Fermi acceleration processes. This will be further illustrated in section 4.

3.2. Size and Parametric Dependence of the Foreshock Bubble

[14] We have examined the effects of the ion beam density, velocity, and width on the strength and size of the foreshock bubble by performing more than 15 separate runs. Beam densities varied between 0.5% and 2% of the solar wind level, while the beam speed varied between 6 and 12 V_A. In all cases, a foreshock bubble was formed with its strength increasing with the beam density or velocity. This indicates that foreshock bubbles should form under all typical solar wind conditions, provided the discontinuity has appropriate geometry.

[15] To understand the scaling properties of the size of the foreshock bubble, we have used ion beams with widths of 100, 200 and 300 ion skin depths. Figure 4 compares the density from these runs at Ωt = 50 for beam density of 2% and velocity of 12 V_A. It is evident that the overall structure of the foreshock bubble does not change with the width of the ion beam. Similarly, in all three cases the size of the foreshock bubble along the X direction remains the same. On the other hand, the size of the bubble along the Y direction scales with the width of the ion beam. This scaling property can be understood when considering the formation mechanism of the foreshock bubble. Upon encountering the discontinuity, the ion beam is deflected due to the change in the magnetic field direction and gyration about this field. The coupling between the solar wind and the deflected ion beam takes place through both the motional electric field and the generation of ULF waves and results in the deceleration of the solar wind. In effect, the interaction acts like a piston and launches a shock wave with a width comparable to that of the ion beam. This shock wave expands sunward with time as the foreshock bubble is convected by the solar wind. As a result, the size of the foreshock bubble along the X direction

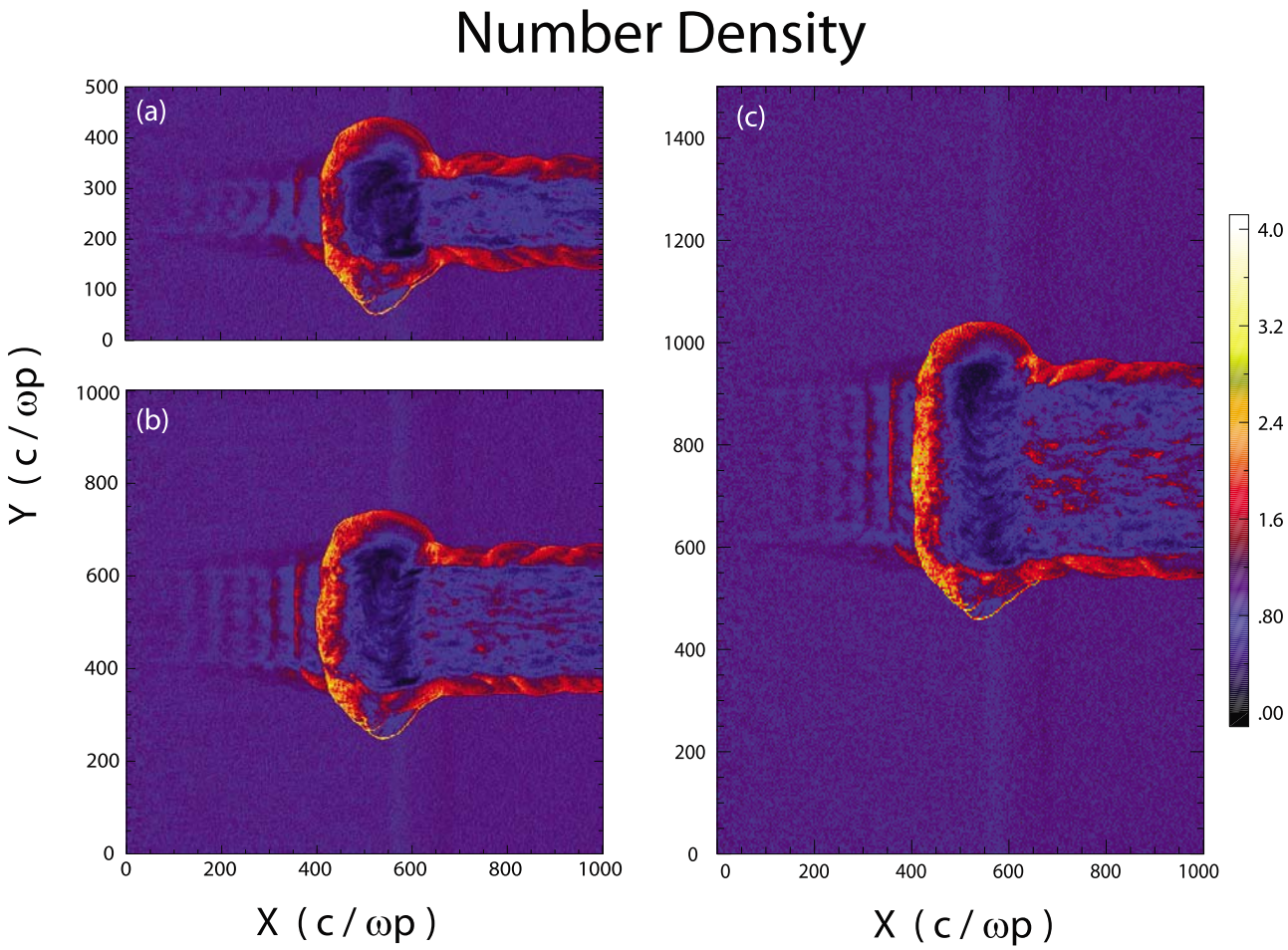

Figure 4. Plots of density from three runs with beam width of (a) 100 ion skin depths, (b) 200 ion skin depths, (c) 300 ion skin depths.

increases with time. Given that Figure 4 corresponds to the same time in the simulation, the size along the X direction is the same despite the differences in the beam width. In short, the size of the foreshock bubble transverse to the flow direction is determined by the width of the ion foreshock (i.e., tens of R_E at the Earth) while the width along the flow direction is determined by its age. We note that given the scaling properties of FBs in the transverse direction to the flow, the ratio of FB size to the magnetosphere is similar in the global simulations discussed in section 4 and at Earth (or any other planet for that matter).

3.3. Effects of the Cone Angle and the Characteristics of the Discontinuities

[16] As mentioned above, the foreshock bubble forms over a wide range of solar wind velocities and ion beam densities. When considering the effects of the magnetic field direction, both the cone angle and the properties (such as direction of the normal and field changes) of the discontinuities in the solar need to be examined. The cone angle is the primary indicator of whether a foreshock bubble formed in the solar wind will collide with the bow shock and magnetosphere. For this collision to take place, the foreshock should be located upstream of the dayside bow shock as opposed to its flanks. This happens during small cone angles. Regarding the impact of the direction of the normal to the discontinuity, a detailed investigation remains to be performed in the future. In general, we would expect the formation of the foreshock bubble to be favored when the angle between the normal and solar wind flow is small or intermediate. This is in contrast to HFAs whose formation is favored during large angles between the normal and flow direction. Given the wide range of possibilities associated with the change in the magnetic field direction at the discontinuity, a comprehensive study is beyond the scope of this paper and remains to be performed in the future. Based on our preliminary examination of this issue, it seems that the foreshock bubble formation is not very sensitive to the details of the change in the magnetic field direction as long as it results in the deflection and gyration of the ion beam.

[17] In order to illustrate that foreshock bubbles are generated over a wide range of cone angles, Figure 5 shows the density from three runs corresponding to the same beam density, velocity, and width as in Figure 1 but cone angles of 30°, 40°, and 50°. Specifically to the right of the RD, the IMF lies in the X-Y plane with the specified cone angle; on the left side of the RD, the IMF lies in the X-Z plane corresponding to the rotation of the Y component of the magnetic field by 90°. Figure 5 also shows the projection of the magnetic field lines in the X-Y plane. It is evident from

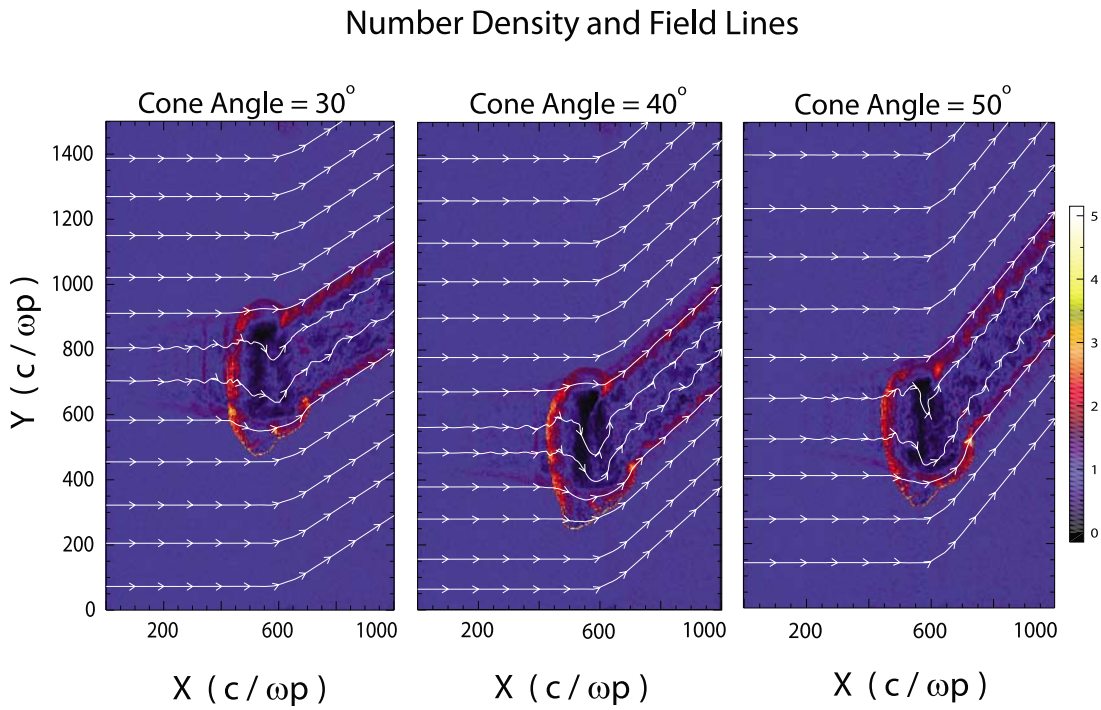

Figure 5. Density and the projection of the magnetic field lines in the *X*-*Y* plane show the formation of foreshock bubbles at cone angles of 30°, 40°, and 50°.

Figure 5 that a foreshock bubble with structure similar to that in Figure 1 forms over a broad range of cone angles.

4. Magnetospheric Consequences

[18] In this section, we present results from a global simulation that starts with a radial IMF geometry. Once a semisteady magnetosphere is formed, we launch a discontinuity from $X = 40$ in the solar wind. Behind the discontinuity, a Z component of the magnetic field with 50% strength of the radial field is present. This allows for a self-consistent formation of a foreshock bubble and its interaction with the bow shock and the magnetosphere.

[19] Before discussing this interaction, we examine the state of the magnetosphere prior to the arrival of the FB at the bow shock. Figure 6 shows the density and magnetic

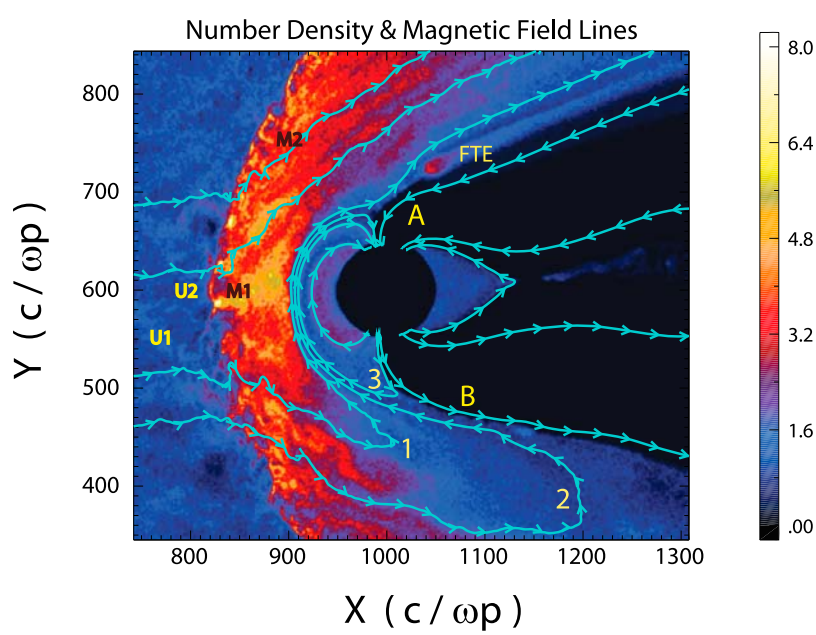

Figure 6. Density and magnetic field lines from the global simulation zoomed around dayside bow shock. Magnetic reconnection occurs at locations labeled A and B.

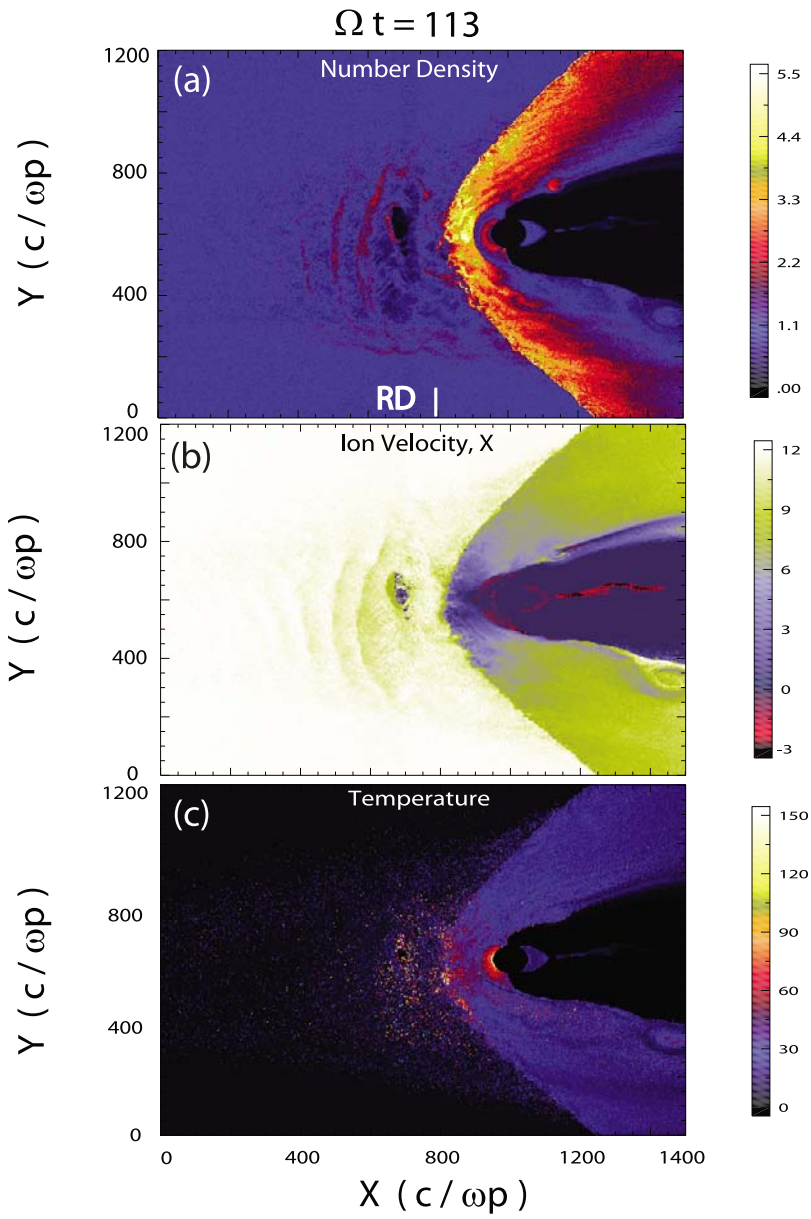

Figure 7. Plots of (a) density, (b) flow speed along *X*, and (c) ion temperature from the global run at the time shown on the top. Figures 7–11 show the evolution of the collision between the foreshock bubble and the magnetosphere.

field lines zoomed around the magnetopause and dayside bow shock in the noon–midnight meridian plane. Upstream of the bow shock, the field lines are generally radial but show variations in direction due to the presence of ULF waves. At the bow shock, the fields in the northern hemisphere are turned northward and in the southern hemisphere southward. Further into the magnetosheath the fields are more complex due to wrapped around the magnetopause and also reconnection at high latitudes labeled A and B in Figure 6. In the absence of solar wind flow and the bow shock, the superposition of the radial field with the dipole field results in reconnection with the night side field in the northern hemisphere and the dayside dipolar field in the southern hemisphere. It is evident that the later reconnection site is carried tailward by the sheath flow. The three field lines labeled 1–3 show the different types of field lines produced in this interaction. The field line 1 is open at both ends, while field line 2 is open at one end and closed at the other, and field line 3 is closed at both ends but is elongated toward the tail due to reconnection in the southern hemisphere. Time-dependent reconnection in both hemispheres results in the formation of flux transfer events (FTEs) [*Russell and Elphic*, 1979] that propagate tailward along the magnetopause surface. One such FTE can be seen in Figure 6 in the northern hemisphere. Although the cause(s) of time dependence of reconnection remain to be established, they are likely tied to the large fluctuations in the density and magnetic field associated with the ULF waves and nonlinear structures in the magnetosheath. This time-dependent reconnection results in time-dependent injection of ions into

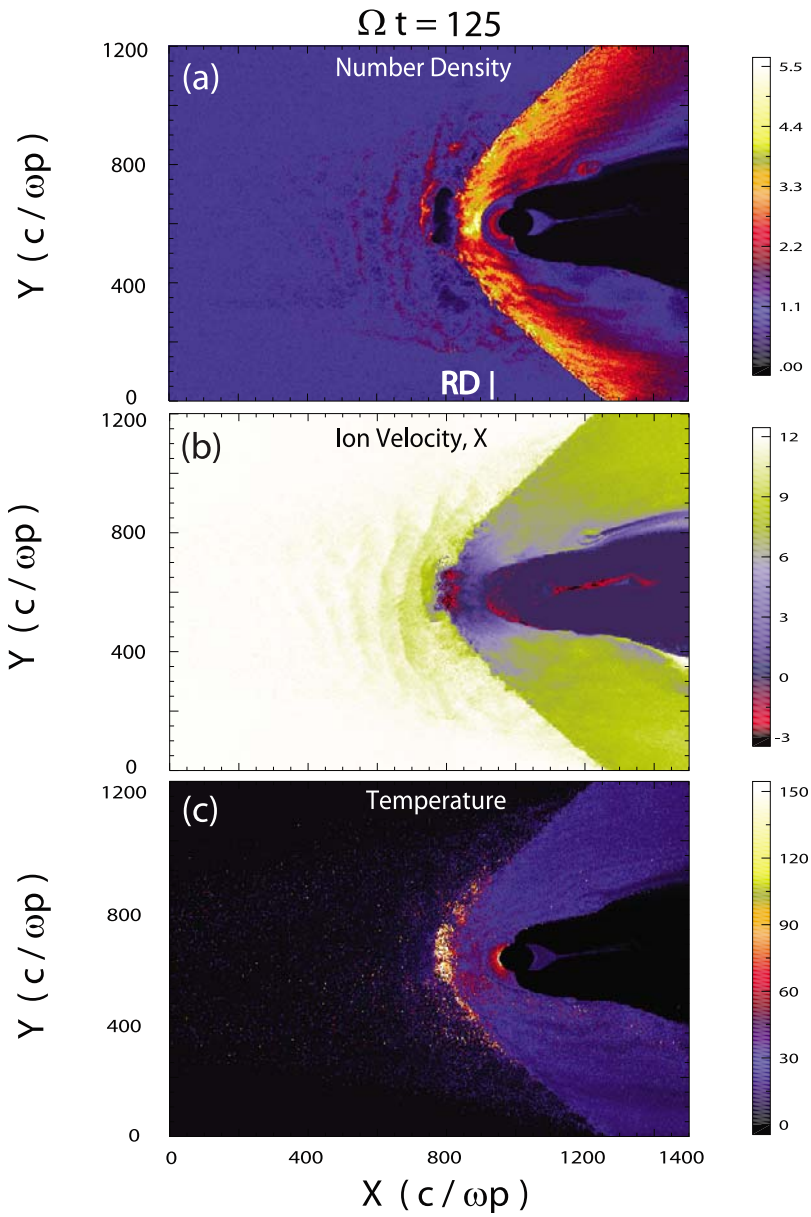

Figure 8. Plots of (a) density, (b) flow speed along X, and (c) ion temperature from the global run at the time shown on the top. Figures 7–11 show the evolution of the collision between the foreshock bubble and the magnetosphere.

the cusp. Finally, Figure 6 shows the presence of a density enhancement in the dayside magnetosphere and lower L shells associated with a population of trapped ions.

[20] Figure 7 shows the density, flow velocity in the X direction, and ion temperature, respectively, at Ωt = 113 when the foreshock bubble is upstream of the bow shock and has not interacted with it. The short white line in the lower portion of Figure 7a shows the location of the RD at this time. We note, however, that upon encountering the bow shock the RD is modified and is no longer a straight line parallel to the Y axis. The lower levels of density and flow speed within the core of the foreshock bubble are evident. Similarly, the presence of high-energy ions in the core of the FB can be seen in Figure 7c which shows high-energy ions not just between the foreshock bubble and the bow shock but also downstream. The spatial extent of these ions in the Y direction is similar to that of the foreshock bubble. This is consistent with the results in the previous section which suggested that foreshock bubbles are highly efficient in particle acceleration through Fermi processes. We note that at this time the flow in the magnetosheath is antisunward as expected.

[21] Figures 8–11 are similar in format to Figure 7 and show the evolution of the system as the magnetosphere responds to the collision with the foreshock bubble and recovers from it. Figure 8 corresponds to Ωt = 125 when the foreshock bubble has begun interacting with the bow shock and the magnetosheath begins to respond to this collision. This response is most evident in Figure 8b which shows sunward flows in the nose regions of the magnetosheath.

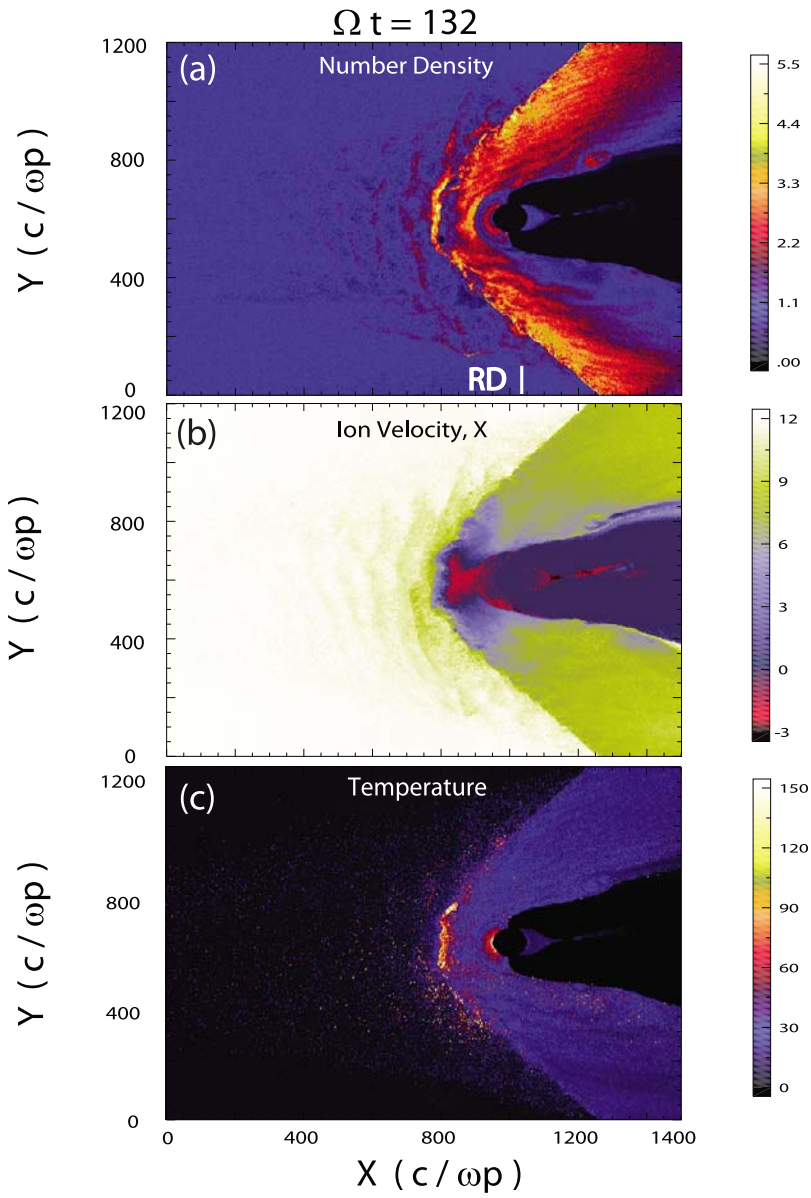

Figure 9. Plots of (a) density, (b) flow speed along X, and (c) ion temperature from the global run at the time shown on the top. Figures 7–11 show the evolution of the collision between the foreshock bubble and the magnetosphere.

Figure 8c shows further acceleration of the energetic ions as they are about to enter into the magnetosheath. Figure 9 corresponds to Ωt = 132 when the interaction between the FB and the magnetosphere is ongoing. Figure 9b illustrates, at this time the dayside magnetosheath flow is sunward which in turn results in the outward motion of the magnetopause and the expansion of the dayside magnetosphere. The sunward motion of the magnetosheath begins when the core of the foreshock bubble reaches the bow shock and the magnetosheath. It is caused by the larger pressure of the magnetosheath plasma as compared to the core plasma and the expansion of the former into the core region. The expansion of a segment of the bow shock and magnetosheath into the core region results in eventual dissipation of that segment of the bow shock and its replacement with the FB shock wave.

[22] Figure 10 corresponds to Ωt = 145 when the foreshock bubble is entirely within the magnetosheath. By this time the magnetopause has moved sunward, and the magnetosphere has expanded resulting in a drop in the density of trapped ions as shown in Figure 10a. During the expansion, the nose of the magnetopause moves 25 ion skin depths in 11 ion gyroperiods which implies a velocity of 2.3 V_A or 230 km/s assuming solar wind Alfven speed of 100 km/s. Figure 10 also shows that some regions of the dayside magnetosheath are associated with high densities and that regions of very low density exist and are associated with the presence of high-energy particles. Figure 10c demonstrates the presence of high-energy particles throughout the dayside magnetosheath, some of which enter the cusp regions. Note that the energy of the trapped ions has been reduced due to the expansion of the magnetosphere. The expansion of the

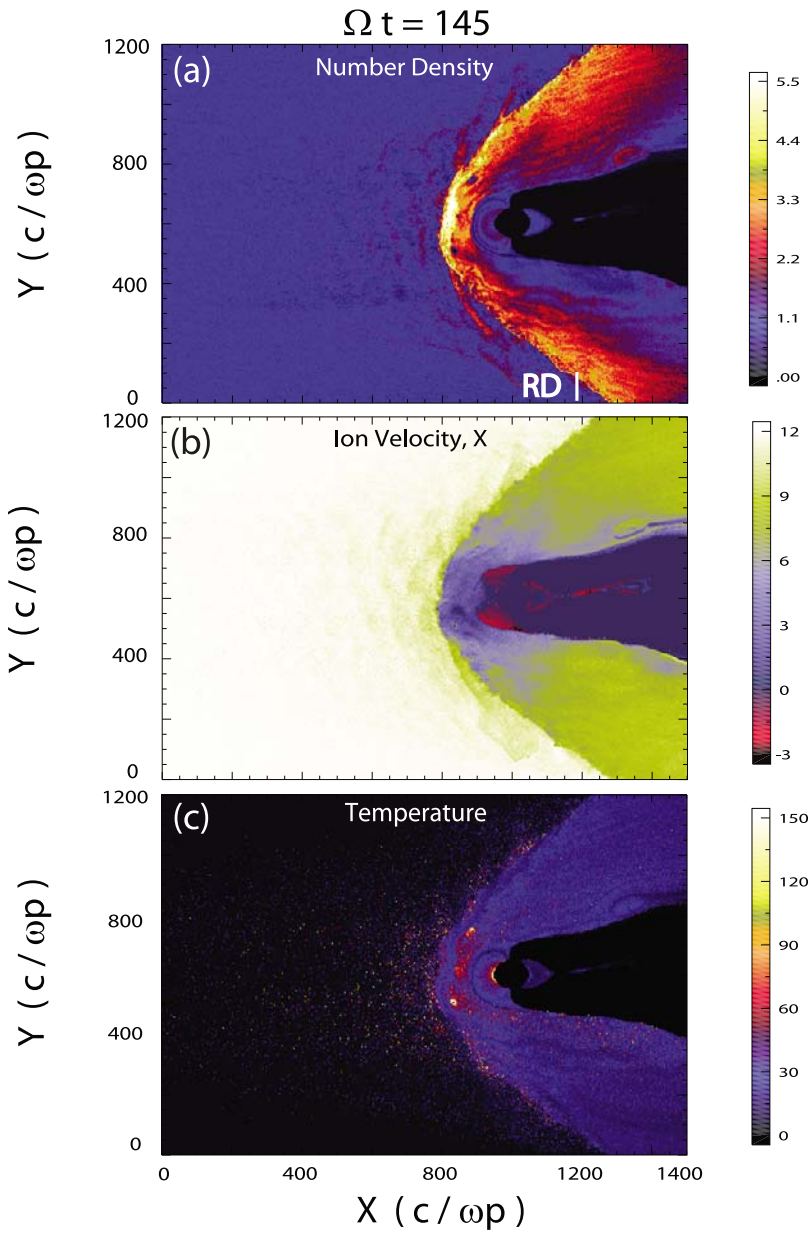

Figure 10. Plots of (a) density, (b) flow speed along X and (c) ion temperature from the global run at the time shown on the top. Figures 7–11 show the evolution of the collision between the foreshock bubble and the magnetosphere.

magnetosphere also disrupts the injection of plasma into the cusps due to high-latitude reconnection. Although in Figure 10 the magnetosphere is in an expanded phase, the magnetosheath flows have returned to an antisunward direction, which in time push the magnetopause back to its original semiequilibrium position.

[23] Figure 11 corresponds to $\Omega t = 175$ and shows that the magnetosphere has for the most part recovered and responded to the new direction of the IMF. However, the two density depletion regions associated with high-energy particles formed during the FB collision are still present in the magnetosheath (one at $X \sim 1{,}050$ and $Y \sim 800$ and the other at $X \sim 1{,}000$ and $Y \sim 400$). These are highly nonlinear structures that are associated with a drop in density by a factor of 10 or more and a correlated increase in the magnetic field by factors of 2–7. They are also associated with flow diversion and acceleration. Given the anticorrelation between the density and the magnetic field of these structures and the fact that the magnetic field is larger than background levels (contrary to the mirror mode waves), we identify them as slow mode structures. The observed size of these structures varies as they evolve and is roughly between 50 and 100 ion skin depths (~5,000–10,000 km).

[24] Figures 7–11 show the presence and propagation of FTEs along the night side magnetopause in both northern and southern hemispheres. Examination of the magnetopause during the interaction with the foreshock bubbles shows that no reconnection occurs in the northern hemisphere. It resumes, however, once the interaction has completed ($\Omega t \sim 180$). In the southern hemisphere, sporadic

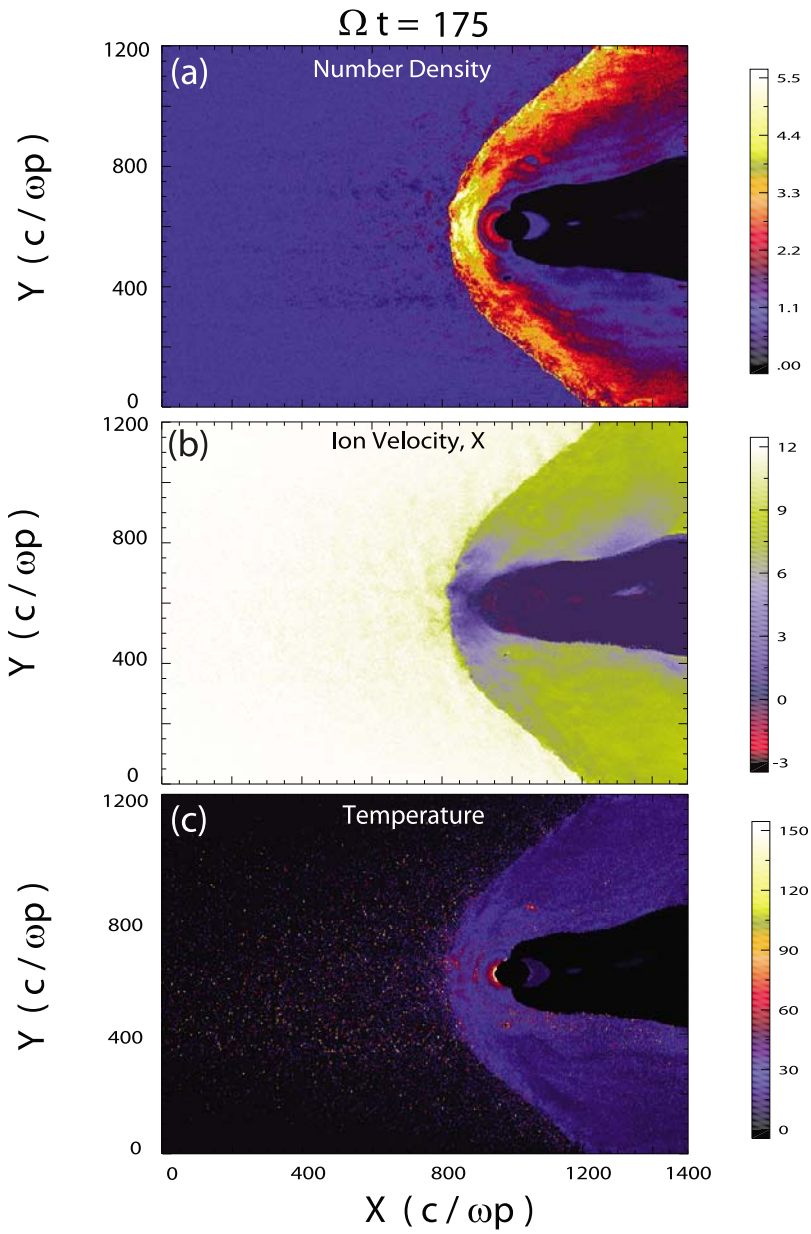

Figure 11. Plots of (a) density, (b) flow speed along X, and (c) ion temperature from the global run at the time shown on the top. Figures 7–11 show the evolution of the collision between the foreshock bubble and the magnetosphere.

reconnection occurs during the collision process; however, the reconnection site moves farther tailward during the interaction. This demonstrates that magnetic reconnection and thereby plasma transport at the magnetopause are greatly impacted by the interaction with the foreshock bubble.

[25] In order to assist with the future identification of FBs in spacecraft data, we show in Figures 12 and 13 time series data from upstream and in the magnetosheath, respectively, during the time interval $\Omega t = 100$–175 which corresponds to ~1.5 min. We would expect the event durations at Earth to be longer by a factor of 5–10 due to the larger size of the magnetosphere. Figure 12 (left) correspond to an observer location of $X = 775$, $Y = 550$, whereas Figure 12 (right) correspond to $X = 800$, $Y = 600$ (marked as U1 and U2 in Figure 6) both of which fall in the upstream region. Both locations show drops in density and flow speed and an increase in temperature associated with the core region of the foreshock bubble around $\Omega t \sim 125$. However, in Figure 12 (left) the flow velocity falls faster and to a lower value than that in Figure 12 (right). An even more significant difference between the two locations is the signature of the magnetic field. Even though Figure 12 (left) shows that no sign of magnetic cavity associated with the FB core is present, Figure 12 (right) shows a clear drop in the magnetic field strength. This contrast is due to changes in the FB that take place close to the bow shock due to ULF waves where some regions of the core are associated with larger than back-

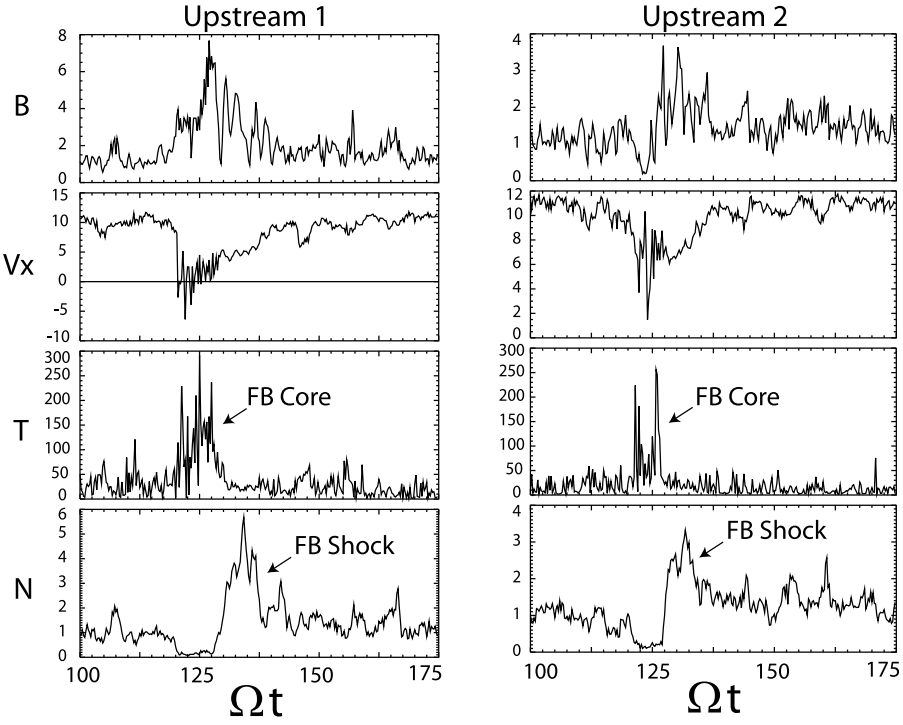

Figure 12. Plots of magnetic field strength, flow speed, temperature, and density as a function of time at two locations upstream of the bow shock.

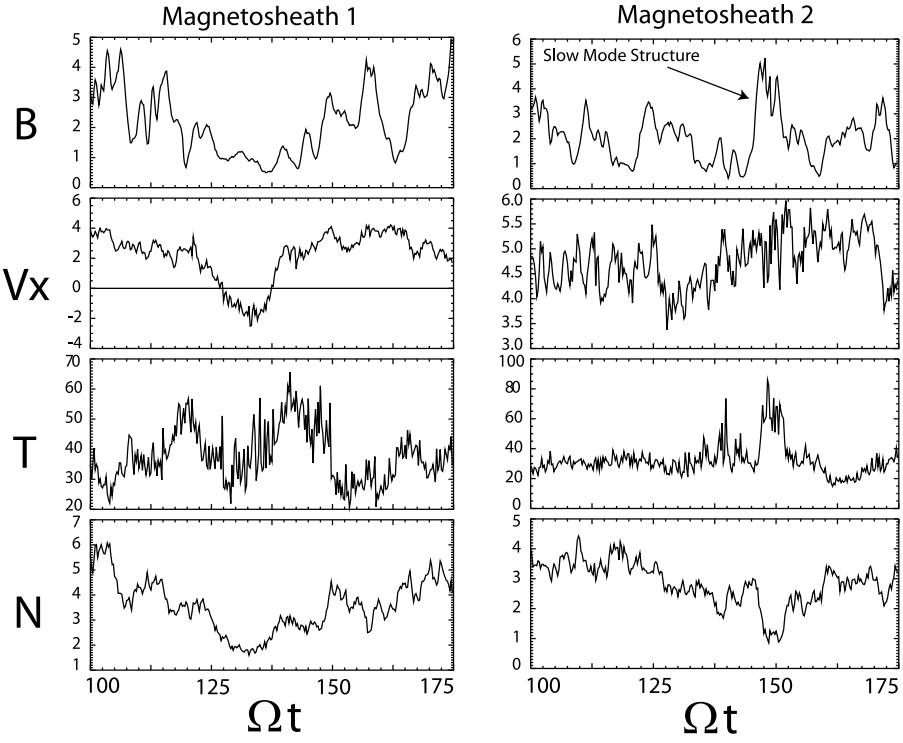

Figure 13. Plots of magnetic field strength, flow speed, temperature, and density as a function of time at two locations in the magnetosheath.

ground field values. After the passage of the core region, both locations observe the fast shock associated with the foreshock bubble and the ULF waves upstream of it.

[26] Figures 13 (left) corresponds to locations $X = 850$, $Y = 600$, and Figure 13 (right) corresponds to locations $X = 900$, $Y = 750$ marked as M1 and M2, respectively, in Figure 6. The signatures observed at these locations in the magnetosheath are considerably different. In Figure 13 (left), the magnetosheath is highly disturbed by the interaction as evidenced in drops in the magnetic field strength, flow velocity, and density. The reversal of the flow from antisunward to sunward and back to antisunward due to the interaction is quite evident. The ion temperature has a more complex structure, and although it is generally higher within the low field and density region, it also has a double peak structure. Figure 13 (right) shows a less subdued response to the interaction by the magnetosheath in that both the field and plasma properties change left than in Figure 13 (less). The most noticeable sign of the FB interaction is the presence of the slow mode structure around $\Omega t \sim 150$ which shows clear enhancements of the magnetic field and temperature and a drop in density.

5. Summary and Conclusions

[27] We presented results from local and global hybrid simulations that show the formation of a new structure called the foreshock bubble. Bubbles form as a result of the interaction between the backstreaming ions in the foreshock and solar wind discontinuities associated with a change in the magnetic field direction. The outer layer of the foreshock bubble corresponds to a bow shock and the associated heated and decelerated solar wind downstream of the shock. The core region of the foreshock bubble consists of less-dense and hotter plasma as compared to the solar wind and is also associated with a drop in the magnetic field strength. Both density and magnetic field fluctuations associated with the ULF waves in the core are also present. Foreshock bubbles are carried by the solar wind in the antisunward direction.

[28] To understand the dependence of the foreshock bubble properties on ion beam density, velocity, and width, we used local hybrid simulations. The results show that foreshock bubbles form over a wide range of beam densities and velocities appropriate for the bow shock and that their strength increases with enhancements in either. The size of the bubble transverse to the solar wind flow direction scales with the width of the ion foreshock. On the other hand, the size of the foreshock bubble along the flow increases with time due to sunward expansion of the structure, and thus, it scales with its age. This scaling property implies transverse FB size of tens of R_E at Earth.

[29] Using local hybrid simulations, we also demonstrated that foreshock bubbles form over a wide range of cone angles. They are expected to impact the magnetosphere the most during smaller cone angles when the foreshock falls upstream of the magnetosphere. It has been shown that the structure of the foreshock bubble remains essentially the same regardless of the cone angle. Similarly, based on the results we have obtained so far, the formation of the foreshock bubble and its structure does not depend on the detailed structure of the discontinuity as long as the change in the magnetic field direction is sufficient to deflect the ion beam. A more detailed examination of this point, however, is desired in future studies. Regarding the impact of the direction of the discontinuity normal, we have only considered direction along the solar wind flow, and more studies are needed in the future to examine this issue. Our expectations are that foreshock bubbles would form over a wide range of angles between the solar wind flow and the discontinuity normal. However, when this angle becomes large, foreshock bubbles may not form. We also expect that the impact of the normal direction of the discontinuity would be affected by the directions of the IMF ahead and behind the discontinuity and the nonradial component of the solar wind velocity. This dependence of the foreshock bubble formation is in contrast to that of HFAs where a large angle between the flow velocity and the discontinuity normal is thought to enhance the interaction.

[30] In this study we showed that foreshock bubbles are highly efficient in particle acceleration. This occurs because a large fraction of the ion beam is reflected by the foreshock bubble as it is convected by the solar wind. In other words, it forms a moving reflecting wall that results in particles going back and forth between the bow shock and the foreshock bubble. This reflecting wall plus the presence of large amplitude ULF waves allows for both first- and second-order Fermi acceleration processes to operate resulting in significant acceleration of ions. Given that the size of the FB perpendicular to the flow scales with the width of the foreshock, we expect the formation of very large foreshock bubbles at astrophysical shocks that should play a significant role in particle acceleration.

[31] Using global hybrid simulations, we examined the self-consistent formation of the foreshock bubble and its interaction with the magnetosphere. The results show that the collision of the FB with the bow shock results in sunward flows in the magnetosheath and the outward motion of the magnetopause. Magnetic reconnection at high latitudes is also affected such that no reconnection is observed in the northern hemisphere during the collision process and the reconnection site in the southern hemisphere is pushed further tailward. As a result, plasma injection into the cusps due to reconnection is affected during the collision. The interaction between the FB and the bow shock injects high-energy ions into the magnetosheath, some of which end up in the cusps. Some of the energetic ions are associated with highly nonlinear slow mode structures that form in the magnetosheath as a result of the collision. They are associated with large drops in the density and large enhancements of the temperature and magnetic field. Their size varies to some extent (5,000–10,000 km) from event to event and also evolves as they move in the magnetosheath. Finally, the results show that the interaction between the FB and the bow shock and the expansion of the dayside magnetosphere results in a drop in density and energy of the trapped ion population in the inner magnetosphere consistent with the behavior of ions that were energized through the betatron process.

[32] This paper presents the first model prediction of structures that form in the foreshock and can impact the magnetosphere in a significant way. Although more theoretical and modeling work remains to be done, examination of spacecraft data for evidence for the existence of such

structures is even more important. As of now, we can mention two sets of observations reported in the literature that could have connection to foreshock bubbles. *Louarn et al.* [2003] report Cluster observations of transient signatures in the dayside magnetosheath that are associated with low density and high energy plasma and changes in the magnetic field and flow direction. These events are also associated with the presence of solar wind discontinuities. *Louarn et al.* [2003] have suggested that these structures form due to the interaction between solar wind discontinuities and the bow shock. The presence of the energetic ions (30 keV) has been attributed to Fermi acceleration processes. *Shue et al.* [2009] report even more intriguing THEMIS observations of sunward flows in the subsolar magnetosheath. Consistent with our model for foreshock bubbles, corresponding ACE observations indicate the presence of two interplanetary RDs during an interval of strongly radial IMF orientation. The two RDs could have resulted in the formation of one or two FBs, which could then have been blown downstream into the bow shock, resulting in the observed sunward magnetosheath flows. Based on private communications with J. H. Shue, we believe this event is a strong candidate for evidence of FB formation and interaction with the bow shock; however, more detailed analysis is needed to confirm this possibility.

[33] **Acknowledgments.** We wish to thank J. H. Shue for helpful discussions of their recent observations. Work for this project was supported by NASA grant NNX08AF38G to Solana Scientific Inc. and GSFC, and NSF grant ATM-0502992.

[34] Zuyin Pu thanks the reviewers for their assistance in evaluating this paper.

References

Asbridge, J. R., S. J. Bame, and I. B. Strong (1968), Outward flow of protons from the earth's bow shock, *J. Geophys. Res.*, *73*, 5777, doi:10.1029/JA073i017p05777.

Blanco-Cano, X., N. Omidi, and C. T. Russell (2006a), Macrostructure of collisionless bow shocks: 2. ULF waves in the foreshock and magnetosheath, *J. Geophys. Res.*, *111*, A10205, doi:10.1029/2005JA011421.

Blanco-Cano, X, N. Omidi, and C. T. Russell (2006b), ULF waves and their influence on bow shock and magnetosheath structures, *Adv Space. Res.*, *37*, 1522–1531, doi:10.1016/j.asr.2005.10.043.

Blanco-Cano, X., N. Omidi, and C.T. Russell (2009), Global hybrid simulations: Foreshock waves and cavitons under radial interplanetary magnetic field geometry, *J. Geophys. Res.*, *114*, A01216, doi:10.1029/2008JA013406.

Bonifazi, C., A. Egidi, G. Moreno, and S. Orsini (1980a), Backstreaming ions outside the earth's bow shock and their interaction with the solar wind, *J. Geophys. Res.*, *85*, 3461–3472, doi:10.1029/JA085iA07p03461.

Bonifazi, C., G. Moreno, A. J. Lazarus, and J. D. Sullivan (1980b), Deceleration of the solar wind in the earth's foreshock region: Isee 2 and Imp 8 observations, *J. Geophys. Res.*, *85*, 6031–6038.

Burgess, D. (1989), On the effect of a tangential discontinuity on ions specularly reflected at an oblique shock, *J. Geophys. Res.*, *94*, 472–478, doi:10.1029/JA094iA01p00472.

Burlaga, L. F. (1969), Directional discontinuities in the interplanetary magnetic field, *Solar Phys.*, *7*, 54–71, doi:10.1007/BF00148406.

Eastwood, J. P., A. Balogh, E. A. Lucek, C. Mazelle, and I. Dandouras (2005), Quasimonochromatic ULF foreshock waves as observed by the four-spacecraft Cluster mission: 1. Statistical properties, *J. Geophys. Res.*, *110*, A11220, doi:10.1029/2004JA010618.

Eastwood, J. P., et al. (2008), Themis observations of a hot flow anomaly: Solar wind, magnetosheath, and ground-based measurements, *Geophys. Res. Lett.*, *35*, L17S03, doi:10.1029/2008GL033475.

Facskó, G., K. Kecskeméty, G. Erdös, M. Tátrallyay, P. W. Daly, and I. Dandouras (2008), A statistical study of hot flow anomalies using Cluster data, *Adv. Space Res.*, *41*, 1286–1291, doi:10.1016/j.asr.2008.02.005.

Fuselier, S. A. (1995), Ion distributions in the Earth's foreshock upstream from the bow shock, *Adv. Space Res.*, *15*, 43–52, doi:10.1016/0273-1177(94)00083-D.

Gosling, J. T., J. R. Asbridge, S. J. Bame, G. Paschmann, and N. Sckopke (1978), Observations of two distinct populations of bow shock ions in the upstream solar wind, *Geophys. Res. Lett.*, *5*, 957–960, doi:10.1029/GL005i011p00957.

Greenstadt, E. W., et al. (1968), Correlated magnetic field and plasma observations of the Earth's bow shock, *J. Geophys. Res.*, *73*, 51–60, doi:10.1029/JA073i001p00051.

Greenstadt, E. W., C. T. Russell, and M. Hoppe (1980), Magnetic field orientation and suprathermal ion streams in the earth's foreshock, *J. Geophys. Res.*, *85*, 3473–3479, doi:10.1029/JA085iA07p03473.

Hoppe, M. M., C. T. Russell, L. A. Frank, T. E. Eastman, and E. W. Greenstadt (1981), Upstream hydromagnetic waves and their association with backstreaming ion populations: ISEE 1 and 2 observations, *J. Geophys. Res.*, *86*, 4471–4492, doi:10.1029/JA086iA06p04471.

Jacobsen, K. S., et al. (2009), THEMIS observations of extreme magnetopause motion caused by a hot flow anomaly, *J. Geophys. Res.*, *114*, A08210, doi:10.1029/2008JA013873.

Lapenta, G. (2002), Particle rezoning for multidimensional kinetic particle-in-cell simulations, *J. Comput. Phys.*, *181*, 317–337.

Lin, Y. (1997), Generation of anomalous flows near the bow shock by its interaction with interplanetary discontinuities, *J. Geophys. Res.*, *102*(A11), 24,265–24,281, doi:10.1029/97JA01989.

Lin, Y. (2002), Global hybrid simulation of hot flow anomalies near the bow shock and in the magnetosheath, *Planet. Space Sci.*, *50*(5–6), 577–591, doi:10.1016/S0032-0633(02)00037-5.

Lin, Y. (2003), Global-scale simulation of foreshock structures at the quasi-parallel bow shock, *J. Geophys. Res.*, *108*(A11), 1390, doi:10.1029/2003JA009991.

Louarn, P., et al. (2003), Observation of energy-time dispersed ion structures in the magnetosheath by CLUSTER: Possible signatures of transient acceleration processes at shock, *Ann. Geophys.*, *21*, 1483–1495.

Lucek, E. A., et al. (2004), Cluster observations of hot flow anomalies, *J. Geophys. Res.*, *109*, A06207,doi:10.1029/2003JA010016.

Mazelle, C., K. Meziane, M. Wilber, and D. Le Queau (2007), Wave-particle interaction in the terrestrial foreshock: New results from Cluster, *AIP Conf. Proc.*, *932*, 175.

Omidi, N. (2007), Formation of foreshock cavities, *AIP Conf. Proc.*, *932*, 181.

Omidi, N., and D. Sibeck (2007), Formation of hot flow anomalies and solitary shocks, *J. Geophys. Res.*, *112*, A01203, doi:10.1029/2006JA011663.

Omidi, N., et al. (2004), Dipolar magnetospheres and their characterization as a function of magnetic moment, *Adv. Space Res.*, *33*, 1996–2003, doi:10.1016/j.asr.2003.08.041.

Omidi, N., X. Blanco-Cano, and C. T. Russell (2005), Macrostructure of collisionless bow shocks: 1. Scale lengths, *J. Geophys. Res.*, *110*, A12212, doi:10.1029/2005JA011169.

Omidi, N., X. Blanco-Cano, C. Russell, and H. Karimabadi (2006), Global hybrid simulations of solar wind interaction with Mercury: Magnetospheric boundaries, *Adv. Space Res.*, *38*, 632–638, doi:10.1016/j.asr.2005.11.019.

Omidi, N., T. Phan, and D. Sibeck (2009a), Hybrid simulations of magnetic reconnection initiated in the magnetosheath, *J. Geophys. Res.*, *114*, A02222, doi:10.1029/2008JA013647.

Omidi, N., D. G. Sibeck, and X. Blanco-Cano (2009b), Foreshock compressional boundary, *J. Geophys. Res.*, *114*, A08205, doi:10.1029/2008JA013950.

Paschmann, G., et al. (1979), Association of low-frequency waves with suprathermal ions in the upstream solar wind, *Geophys. Res. Lett.*, *6*, 209, doi:10.1029/GL006i003p00209.

Paschmann, G., et al. (1988), Three-dimensional plasma structures with anomalous flow directions near the Earth's bow shock, *J. Geophys. Res.*, *93*(A10), 11,279–11,294, doi:10.1029/JA093iA10p11279.

Russell, C. T., and R. C. Elphic (1979), ISEE observations of flux transfer events at the dayside magnetopause, *Geophys. Res. Lett.*, *6*, 33, doi:10.1029/GL006i001p00033.

Russell, C. T., and M. Hoppe (1983), Upstream waves and particles, *Space Sci. Rev.*, *34*, 155, doi:10.1007/BF00194624.

Schwartz, S. J., et al. (1988), Active current sheet near the Earth's bow shock, *J. Geophys. Res.*, *93*(A10), 11295–11310.

Schwartz, S. J. (1995), Hot flow anomalies near the earth's bow shock, *Adv. Space Res.*, *15*, 107–116, doi:10.1016/0273-1177(94)00092-F.

Schwartz, S. J., et al. (2000), Conditions for the formation of hot flow anomalies, *J. Geophys. Res.*, *105*(A6), 12,639–12,650, doi:10.1029/1999JA000320.

Shue, J. H., et al. (2009), Anomalous magnetosheath flows and distorted subsolar magnetopause for radial interplanetary magnetic fields, *Geophys. Res. Lett.*, *36*, L18112, doi:10.1029/2009GL039842.

Sibeck, D., N. Borodkova, G. Zastenker, S. Romanov, and J.-A. Sauvaud (1998), Gross deformation of the dayside magnetopause, *Geophys. Res. Lett.*, *25*(4), 453–456, doi:10.1029/98GL00134.

Sibeck, D. G., et al. (1999), Comprehensive study of the magnetospheric response to a hot flow anomaly, *J. Geophys. Res.*, *104*(A3), 4577–4593, doi:10.1029/1998JA900021.

Sibeck, D. G., K. Kudela, R. P. Lepping, R. Lin, Z. Nemecek, M. N. Nozdrachev, T. D. Phan, L. Prech, J. Safrankova, H. Singer, and Y. Yermolaev (2000), Magnetopause motion driven by interplanetary magnetic field variations, *J. Geophys. Res.*, *105*(A11), 25,155–25,169, doi:10.1029/2000JA900109.

Sibeck, D. G., N. Omidi, I. Dandouras, and E. Lucek (2008), On the edge of the foreshock: Model-data comparisons, *Ann. Geophys.*, *26*, 1539.

Thomas, V., et al. (1991), Hybrid simulation of the formation of a hot flow anomaly, *J. Geophys. Res.*, *96*(A7), 7779–7791, doi:10.1029/91JA01092.

Thomsen, M. F., et al. (1986), Hot diamagnetic cavities upstream of the earth's bow shock, *J. Geophys. Res.*, *91*, 2961.

Thomsen, M. F., et al. (1988), On the origin of hot diamagnetic cavities near the Earth's bow shock, *J. Geophys. Res.*, *93*(A10), 11,311–11,325, doi:10.1029/JA093iA10p11311.

Thomsen, M. F., et al. (1993), Observational test of hot flow anomaly formation by the interaction of a magnetic discontinuity with the bow shock, *J. Geophys. Res.*, *98*(A9), 15,319–15,330, doi:10.1029/93JA00792.

Winske, D., and N. Omidi (1993), Hybrid codes: Methods and applications, in *Computer Space Plasma Physics: Simulation Techniques and Software*, edited by H. Matsumoto, and Y. Omura, p. 103, Terra Sci., Tokyo.

Winske, D., and N. Omidi (1996), A nonspecialist's guide to kinetic simulations of space plasmas, *J. Geophys. Res.*, *101*(A8), 17287.

J. P. Eastwood, Space Sciences Laboratory, University of California, Berkeley, CA 94720-7450, USA.

N. Omidi, Solana Scientific Inc., Solana Beach, CA 92075, USA. (omidi@solanasci.com)

D. G. Sibeck, NASA Goddard Space Flight Center, Greenbelt, MD 20771, USA.